

# Mode Parity-Controlled Fano- and Lorentz-like Line Shapes Arising in Plasmonic Nanorods

Niels Verellen,<sup>\*,†,‡</sup> Fernando López-Tejiera,<sup>§</sup> Ramón Paniagua-Domínguez,<sup>||</sup> Dries Vercruysse,<sup>‡,†</sup> Denitza Denkova,<sup>†</sup> Liesbet Lagae,<sup>‡,†</sup> Pol Van Dorpe,<sup>‡,†</sup> Victor V. Moshchalkov,<sup>†</sup> and José A. Sánchez-Gil<sup>||</sup>

<sup>†</sup>INPAC and Department of Physics and Astronomy, KU Leuven, Celestijnenlaan 200 D, B-3001 Leuven, Belgium

<sup>‡</sup>IMEC, Kapeldreef 75, B-3001 Leuven, Belgium

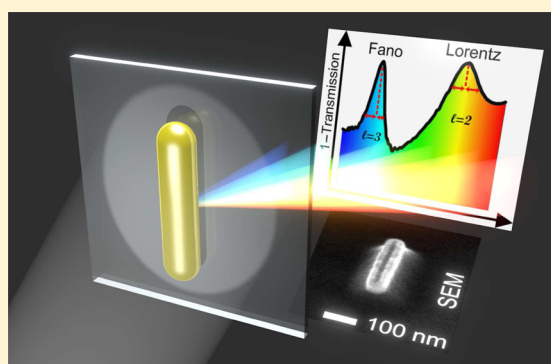
<sup>§</sup>Departamento de Física de la Materia Condensada, Escuela de Ingeniería y Arquitectura, Universidad de Zaragoza, María de Luna 3, E-50018 Zaragoza, Spain

<sup>||</sup>Instituto de Estructura de la Materia (IEM-CSIC), Consejo Superior de Investigaciones Científicas, Serrano 121, E-28006 Madrid, Spain

## S Supporting Information

**ABSTRACT:** We present the experimental observation of spectral lines of distinctly different shapes in the optical extinction cross-section of metallic nanorod antennas under near-normal plane wave illumination. Surface plasmon resonances of odd mode parity present Fano interference in the scattering cross-section, resulting in asymmetric spectral lines. Contrarily, modes with even parity appear as symmetric Lorentzian lines. Finite element simulations are used to verify the experimental results. The emergence of either constructive or destructive mode interference is explained with a semianalytical 1D line current model. This simple model directly explains the mode-parity dependence of the Fano-like interference. Plasmonic nanorods are widely used as half-wave optical dipole antennas. Our findings offer a perspective and theoretical framework for operating these antennas at higher-order modes.

**KEYWORDS:** Nanoantenna, surface plasmon resonance, Fano resonance, interference, plasmonics



Metallic nanorods are exploited as biological imaging probes and widely used as generic plasmonic dipole antennas operating at optical and near-infrared frequencies, forming an analogue to classical half-wave dipole antennas. Nanorod antennas are an excellent tool for the manipulation of a variety of nanoscale light–matter interactions.<sup>1,2</sup> They form the building blocks for Yagi-Uda antennas which allow directional control of light,<sup>3–6</sup> or they can act as active optical antennas for photodetection by generating hot electrons.<sup>7</sup> Recently, it was demonstrated how plasmonic nanorods can be used to efficiently convert the radiation of quantum emitters into novel multipolar sources of photons owing to the higher-order localized surface plasmon resonances (LSPRs) supported by these antennas.<sup>8,9</sup>

The fundamental dipole and higher-order antenna modes have been extensively studied experimentally using optical spectroscopy<sup>10–15</sup> and a broad range of mapping techniques based on, for example, scanning near-field microscopy,<sup>16–19</sup> two-photon induced luminescence (TPL),<sup>20</sup> cathodoluminescence,<sup>21</sup> multiphoton absorption in photosensitive polymers,<sup>22</sup> electron energy loss spectroscopy (EELS),<sup>23</sup> and photocurrent mapping.<sup>24</sup> Likewise, theoretical investigations have elucidated the antenna modes' scaling properties and their dependence on

the shape, size, and dielectric environment by using a variety of methods.<sup>12,13,25–27</sup> Despite this large interest in nanorods, only very few reports—all theoretical—address the scattering behavior with a focus on the spectral line shape.<sup>28–30</sup>

Plasmon resonance, as a wave phenomenon, is expected to present interference characteristics. The wave nature of propagating surface plasmon polaritons (SPPs) was elegantly demonstrated with a Young's double slit experiment.<sup>31</sup> For localized surface plasmon resonances, the interference of spectrally overlapping and coupled modes is well-recognized to affect the scattering behavior of the nanostructure under investigation.<sup>32,33</sup> In particular, the interference of a broad background continuum state with spectrally sharp higher-order resonances, as schematically illustrated in Figure 1a, can lead to a spectral response with asymmetric Fano-like line shapes in a variety of nanoparticle configurations such as nanosphere clusters,<sup>34</sup> asymmetric dolmen-like nanorod arrangements,<sup>35,36</sup> disk-ring arrangements,<sup>37,38</sup> nanocrosses,<sup>39,40</sup> and others.<sup>32,41</sup> Fano resonances can also be substrate-induced in nanorods

**Received:** December 17, 2013

**Revised:** March 28, 2014

**Published:** April 4, 2014

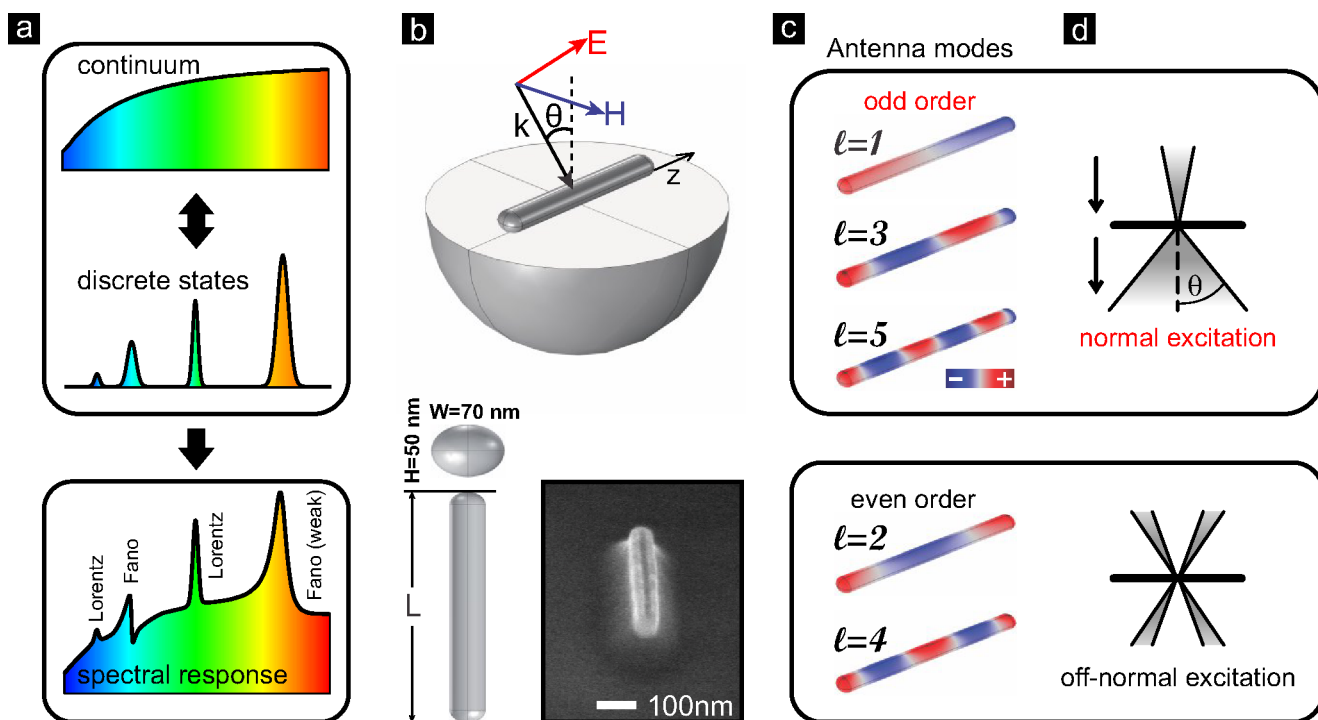


**Figure 1.** (a) Illustration of the coupling process of a broad background continuum state with different discrete states resulting in a complex spectral response including symmetric Lorentzian lines and different asymmetric Fano line shapes. (b) Schematic showing incident plane wave vectors and the modeled nanorod shape with dimensions: width  $W = 70$  nm, height  $H = 50$  nm, and length  $L$ . Right: SEM image of a fabricated nanorod. (c) Simulated charge density distributions for indicated mode order  $l$  ( $L = 720$  nm). Red and blue regions represent positive and negative charges, respectively. (d) Schematic of the experimental extinction measurement configurations to approximate normal and off-normal plane wave illumination.

with a low aspect ratio.<sup>42,43</sup> Only recently, it was indicated that Fano resonances may appear for individual high aspect ratio nanorods provided that interacting modes overlap in both spatial and frequency domains.<sup>28,29,44</sup> The narrow asymmetrical line shape of a nanorod's Fano interference is, for example, more favorable for label-free biosensing than broader Lorentzian resonances,<sup>30</sup> can be essential for slow-light metamaterials due to its strong dispersion,<sup>45</sup> and can be applied for low-loss plasmonic wave guiding.

Here, we study, both theoretically and experimentally, the spectral line shapes of nanorod antennas in detail, using extinction spectroscopy and finite element simulations. When a nanorod is illuminated with light that is polarized along its long axis (as in Figure 1b), charge density waves at the surface of the metal are excited, which can form standing wave-like Fabry-Pérot resonances.<sup>17,46,47</sup> Here, the resonance mode index  $l$  is defined as the number of half plasmon wavelengths  $\lambda_p/2$  that fit the antenna cavity at resonance and coincides with the number of charge nodes in the corresponding charge density distribution. These longitudinal antenna modes can be separated in two categories based on the mirror symmetry of their respective charge density. As shown in Figure 1c, modes of odd parity have an antisymmetric distribution consisting of an odd number of charge nodes  $l$ , while even parity modes are symmetric in their charge distribution and have an even number of charge nodes. As we will show, a distinct spectral behavior is found for even and odd parity modes. First of all, the mode parity strongly determines its coupling to light. For example, even modes will not couple to a p-polarized plane wave that impinges perpendicular to the nanorod's long axis. Retardation of the incident electromagnetic field along the

nanorod's length is required to excite even parity modes, which can be achieved by oblique incidence of the plane wave.<sup>11</sup> It will further be demonstrated that not only the coupling efficiency to plane waves strongly depends on the mode parity, but also the mode's spectral line shape. We will show that odd modes present asymmetric line shapes characteristic for Fano interference, while symmetric Lorentzian lines appear for even modes. By a detailed analysis of calculated absorption and scattering cross-sections (ACS, SCS), destructive and constructive mode interference in nanorod antennas is revealed. The resulting Fano resonance line shapes are experimentally observed for first-, third-, and fifth-order antenna modes and are in excellent agreement with simulations for different rod lengths. The dimensionless factors  $q_i$  that describe both the intensity of resonances and their degree of asymmetry (and are connected with the so-called Fano factor<sup>48</sup>) are determined from a fit to the experimental data. They are found to depend linearly on the antenna length, in agreement with earlier theoretical work.<sup>29</sup> A semianalytical model based on a one-dimensional (1D) wire reproduces the observed line shapes and gives an intuitive understanding of the underlying interference mechanisms.

A scanning electron beam microscopy (SEM) image of the nanorod antennas studied in this work is shown in Figure 1b. The nanostructures consist of sputtered gold with a thickness of 50 nm (= antenna height  $H$ ) and are supported by a glass substrate. They were fabricated using electron beam lithography with negative-tone hydrogen silysequioxane (HSQ) resist, subsequent Xe ion milling, and a sulfur hexafluoride + oxygen dry etch.<sup>39</sup> This last step is applied to remove the remaining resist on top of the particles and etches part of the

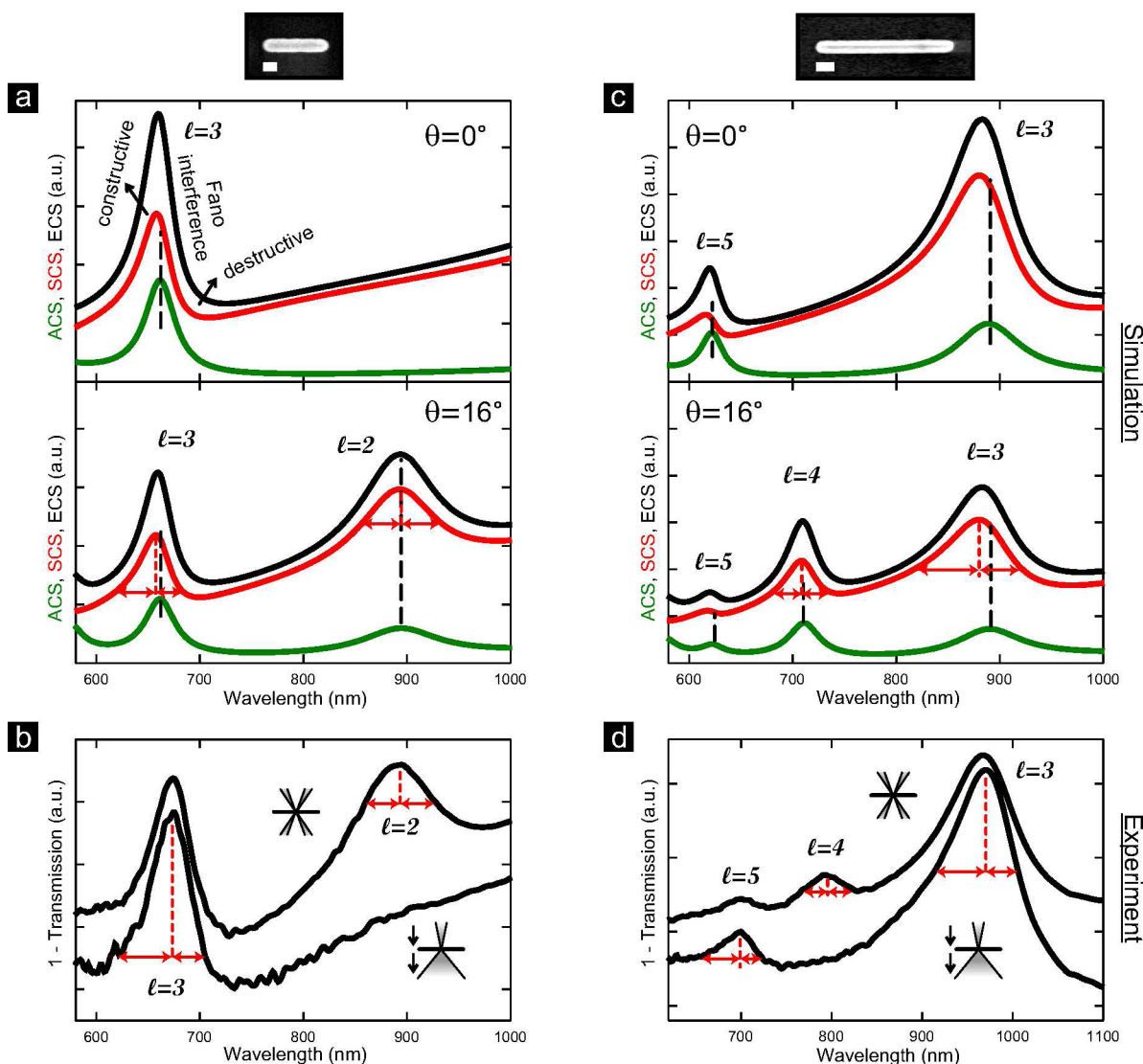


**Figure 2.** Fano interference in nanorod antennas. (a,c) Simulated absorption (ACS, green), scattering (SCS, red), and extinction (ECS, black) cross-sections for  $L = 470$  and  $720$  nm, respectively, under normal excitation ( $\theta = 0^\circ$ , top) and off-normal excitation ( $\theta = 16^\circ$ , bottom). (b,d) Corresponding experimental extinction (1-transmission) spectra measured with normal excitation (bottom curve) and off-normal excitation (top curve) configuration. Red arrows highlight the symmetric and asymmetric spectral line shapes of the resonances. Top insets show SEM images of the antennas; scale bar: 100 nm.

substrate such that the nanorods are mounted on a pillar. The bright rim on top of the particle seen in the SEM image results from gold redeposition during the ion-milling step. The antennas have a width  $W$  of 70 nm and are arranged in  $50 \times 50 \mu\text{m}^2$  square arrays with a pitch of  $2 \mu\text{m}$  in order to avoid near-field coupling and diffraction related effects.

Two measurement configurations, schematically illustrated in Figure 1d, are used to experimentally investigate the nanorods' optical extinction (1-transmission) spectra. Using a low NA = 0.1, 4 $\times$  magnification objective to excite the nanorod sample, a normal incident plane wave is approximated (top configuration). The transmitted light is collected by a 20 $\times$  magnification, NA = 0.45 semiapochromat objective. Rather than tilting the sample,<sup>11</sup> off-normal excitation is achieved by using two identical reflective objectives (15 $\times$  magnification, NA = 0.4) which create (and collect) a light cone with  $10^\circ \lesssim \theta \lesssim 23^\circ$  (bottom configuration). Spectra are taken with a Fourier transform infrared (FTIR) spectrometer equipped with a microscope (Bruker vertex 80v + Hyperion). The light of a

tungsten lamp is polarized, spatially filtered with a metal knife edge aperture, and finally detected with a Si diode detector in the visible/near-IR and a liquid nitrogen cooled mercury-cadmium-telluride (MCT) detector in the near-IR/mid-IR. All spectra are normalized to a reference spectrum taken on the bare substrate under identical conditions.

Extinction, scattering, and absorption spectra, as well as the charge density distribution, are calculated from finite element method (FEM) simulations with the RF module of COMSOL Multiphysics finite element software, version 4.3. The dielectric permittivity of gold is obtained from ellipsometry data of the gold films used in our fabrication process. These data match well the values reported in literature.<sup>49</sup> In the simulations, the nanorods are positioned on a flat substrate with refractive index  $n = 1.524$ . The antennas are modeled as elliptic cylinders ( $H = 50$  nm;  $W = 70$  nm) with hemiellipsoidal ends, as shown in Figure 1b. The antennas are illuminated by a plane wave that impinges with a given angle  $\theta$  and is polarized along the

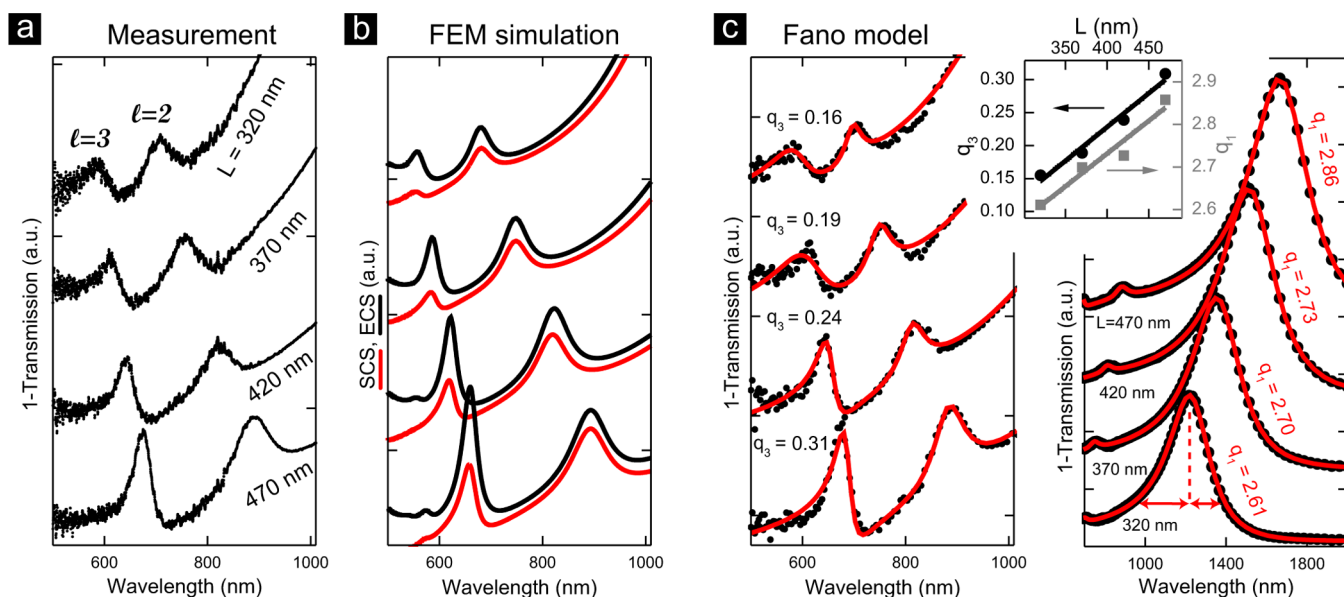


**Figure 3.** Nanorod length variation and phenomenological Fano model fit. (a) Experimental extinction spectra for different nanorod antenna lengths ( $L = 320, 370, 420,$  and  $470$  nm). (b) Corresponding simulated ECS (black) and SCS (red) spectra with a refined angle averaging within  $\theta = 10\text{--}23^\circ$ . Spectra are normalized with respect to the  $l = 1$  dipole mode (outside the shown spectral window) peak intensity and shifted for clarity. (c) Fits (red) to the experimental spectra (black) using the heuristic Fano formula. Left: spectral window showing  $l = 2, 3$ . Right: spectral window showing  $l = 1$  (for clarity, the spectra are shifted oppositely from the previous panels). Inset: extracted Fano factors  $q_l$  for the  $l = 1$  (square symbols) and  $l = 3$  (circle symbols) mode. The y-axes have a different scale.

antenna's long axis. More details can be found in the Supporting Information.

Figure 2a shows the simulated extinction cross-section (ECS, black line), scattering cross-section (SCS, red line), and absorption cross-section (ACS, green line) for a nanorod of length  $L = 470$  nm illuminated by a normal (top,  $\theta = 0^\circ$ ) and off-normal (bottom,  $\theta = 16^\circ$ ) incident plane wave. Normal incidence couples only to odd modes ( $l = 3$  shown), while off-normal incidence results in the excitation of the even order  $l = 2$  mode at  $\lambda = 900$  nm simultaneously with the odd order  $l = 3$  mode at  $\lambda = 670$  nm. When comparing absorption with scattering, the effect of the mode parity on the antenna's spectral behavior becomes evident. In absorption both modes present a symmetric Lorentzian resonance line shape. In the scattering spectrum, however, the odd mode is asymmetric, and the absorption maximum is located at the longer wavelength slope of the scattering resonance. This indicates the occurrence of interference—constructive at the lower wavelength side of the absorption resonance, while destructive at longer wavelengths. This behavior is characteristic for a Fano resonance where a sharp higher-order mode interferes with a broad lower order mode or continuum.<sup>32,48</sup> This result shows that Fano-like interference in the scattering cross-section, which was recently theoretically demonstrated for nanorods of various geometries,<sup>29</sup> persists in the asymmetric dielectric environment introduced by a glass substrate. Note that the current situation is different from the substrate-induced Fano resonances reported in refs 42 and 43 for low aspect ratio nanorods. The high aspect ratio of the investigated rods and relatively low refractive index of the substrate ensure that only longitudinal antenna modes spectrally overlap and contribute to the interference. Figure S1 in the Supporting Information compares the SCS with and without substrates, evidencing that the Fano interference is not substrate-induced.

Experimentally, the light transmitted through the nanorod sample is detected and plotted as 1–transmission. Consequently, the resulting spectrum is a combination of the light intensity absorbed by the antennas and (part of) the light scattered by the antennas. It should therefore be compared to the calculated extinction spectra. Although less pronounced because of the symmetric absorption component, the extinction still shows spectral asymmetry, evidencing the spectral interference contributed by the scattering. Figure 2b shows the experimental extinction spectra of a nanorod array with  $L = 470$  nm. A corresponding SEM image is shown on top of panel a. When measured in the normal plane wave excitation configuration (illustrated in Figure 1d), using a low NA objective lens, only the odd order modes  $l = 3$  at  $\lambda = 670$  nm and  $l = 1$  at  $\lambda = 1650$  nm (outside the displayed spectral window) are excited (bottom curve). In off-normal excitation configuration, as expected, the second-order  $l = 2$  mode appears (top curve). Most importantly, the asymmetric Fano and symmetric Lorentzian line shapes of the  $l = 3$  and  $l = 2$  modes, respectively, are experimentally reproduced.

Since this Fano interference phenomenon is parity related, other odd higher-order modes can be expected to present similar behavior. To get higher-order modes at frequencies above the strongly absorbing gold interband transitions, the nanorod length needs to be increased. The simulated cross-sections for a rod with  $L = 720$  nm is shown in Figure 2c and corresponding resonance charge density distributions in Figure 1c. As was the case for the shorter rod in panel a, the symmetric absorption resonance is located in the longer wavelength slope of the scattering resonance of both the third- and the fifth-order modes, indicating interference. The even fourth-order mode, similarly to  $l = 2$  of the shorter rod, shows a symmetric scattering behavior. The corresponding experimental results are shown in panel d. The asymmetric Fano profiles are clearly

observed in the normal excitation configuration (bottom curve). For the off-normal excitation  $l = 4$  pops up.

In order to reproduce the actual experimental conditions in the simulation model, the full excitation light cone of the reflective objective is taken into account in the simulation results shown in Figure 3b by averaging over the illumination angle within  $\theta = 10\text{--}23^\circ$ . The experimental spectra obtained with off-normal excitation for different antenna lengths  $L$  between 320 and 470 nm (panel a) show excellent agreement with the calculated extinction (black lines). As expected, the relative heights of the resonances are slightly modified by the averaging, giving a good agreement with the experimental relative peak intensities. Corresponding scattering spectra are shown by the red lines. Both the even and the odd modes red shift with increasing  $L$ , as expected for a linear antenna.<sup>25</sup> Individual SCS spectra of the  $L = 470$  nm rod for  $\theta$  ranging from  $0^\circ$  (normal incidence) to  $60^\circ$  (oblique incidence) can be found in Figure S1 in the Supporting Information.

As the next step to a proper understanding of the experimental line shapes, we present in Figure 3c fits to the experimental spectra (black dots) with a heuristic Fano model (red lines) within the energy range encompassing the  $l = 3$  and  $l = 2$  resonances (left) and also the  $l = 1$  resonance (right). Without entering into further details (see Supporting Information), let us say that such a theoretical framework provides an effective and flexible description of the interaction between illumination and longitudinal plasmon resonances in metallic nanorods of different geometries. Quantitatively speaking, the interaction with odd modes is governed by dimensionless real parameters  $q_i$  that account for the line shape asymmetry while simultaneously measure their relative intensity with respect to the finite background. As it has been recently pointed out by other authors,<sup>50,51</sup> this “convolution” makes  $q_i$  to deviate from the precise meaning of the asymmetry factor in the canonical Fano model. However, the obtained agreement is really good, which confirms the overall validity of our approach. From the experimental data and fits in Figure 3c, it can be seen that also the first order ( $l = 1$ ) antenna mode presents an asymmetric Fano line shape—be it weaker than that for  $l = 3$ . FEM simulations of the SCS and ACS including the  $l = 1$  mode are shown in the Supporting Information (Figure S3). The obtained factors  $q_3$  (for  $l = 3$ ) and  $q_1$  (for  $l = 1$ ) are included in panel c and show a linear dependence with nanorod length  $L$  (see inset). This behavior can be summarized as “the more elongated the particle, the more pronounced the resonances” and confirms our previous theoretical results for similar nanorod geometries.<sup>29</sup>

Although really convenient from a practical point of view, the heuristic model lacks any predictive ability for a given system in the absence of previously either measured or calculated spectra. In order to overcome such limitation and to further elucidate the mechanisms giving rise to the Fano interference of the odd-parity modes, we present hereafter a 1D line current model that directly explains the emergence of either constructive or destructive interference as stemming from the mode-parity dependence of the Fano-like interference.

Following ref 47, we assume that a nanorod of length  $L$ , when illuminated by a plane wave of frequency  $\omega$ , as shown in Figure 1b, behaves as an antenna with a current density which can be expressed in terms of the electric field inside the nanorod as

$$\mathbf{I}(\mathbf{x}) = -i\omega\epsilon(\omega)\mathbf{E}^{(\text{inside})}(\mathbf{x}) \quad (1)$$

Note that, in contrast to ref 47, displacement currents are also included in eq 1. For an elongated, thin nanorod located along the  $z$ -axis, such current density is uniform in the transverse plane and can then be written as a 1D line current  $\mathbf{I}(\mathbf{x}) = I(z)\hat{\mathbf{z}}$ , where

$$I(z) = I_{\parallel}e^{ik_{\parallel}z} + I_{p+}e^{ik_p(\omega)z} + I_{p-}e^{-ik_p(\omega)z} \quad (2)$$

The first term is induced by the illuminating field with  $k_{\parallel} \equiv k_0 \sin \theta$  and amplitude  $E_0$ , with

$$I_{\parallel} = -i\omega\epsilon(\omega)\frac{k_p^2(\omega) - k_0^2}{k_p^2(\omega) - k_{\parallel}^2}E_0 \cos \theta \quad (3)$$

The other two terms are counter-propagating plasmons, characterized by the corresponding wavevector  $k_p(\omega)$ , with

$$I_{p+} = -I_{\parallel}\frac{r^2e^{i(k_p+k_{\parallel})L/2} - e^{-i(k_p+k_{\parallel})L/2}}{r^2e^{ik_pL} - e^{-ik_pL}} \quad (4)$$

$$I_{p-} = rI_{\parallel}\frac{e^{i(k_p-k_{\parallel})L/2} - e^{-i(k_p-k_{\parallel})L/2}}{r^2e^{ik_pL} - e^{-ik_pL}} \quad (5)$$

for  $\theta \neq 0$ , and:

$$I_{p\pm} = -I_{\parallel}\frac{r - 1}{2}\frac{re^{ik_pL/2} - e^{-ik_pL/2}}{r^2e^{ik_pL} - e^{-ik_pL}} \quad (6)$$

for  $\theta = 0$ . The reflection coefficients  $r$  account for radiation losses experienced by the plasmon wave upon reflection from the nanorod cavity walls.<sup>8</sup>

Bear in mind that the propagating plasmon dispersion  $k_p(\omega)$  differs from that of a surface plasmon polariton propagating along a metal surface or slab. Rather, it corresponds to the dispersion of the lowest TM mode of an infinitely long cylinder with frequency-dependent permittivity  $\epsilon(\omega)$ . In Figure 4b the (complex) plasmonic mode's dispersion relation ( $k_z = k_p$ ) used in the model is shown, which corresponds to the same cross-sectional shape as that in the FEM full numerical simulations. For our specific nanorod-on-substrate arrangement, the impact of the substrate is approximately taken into account by assuming a homogeneous surrounding medium with an effective refractive index in between that of vacuum and glass.

The electric far-field generated by a current  $\mathbf{I}(\mathbf{x}) = I(z)\hat{\mathbf{z}}$  in the nanorod necessarily exhibits axial symmetry and has the form:

$$E_{\theta_s} = \frac{ik_0\eta_0 S_{\text{rod}}^{xy}}{4\pi} \cos \theta_s \int_{-L/2}^{L/2} I(z) e^{-ik_0z \sin \theta_s} dz \quad (7)$$

where  $\eta_0$  stands for the impedance of the incident medium,  $k_0$  for the incident wavevector,  $S_{\text{rod}}^{xy} = \pi WH/4$  for the geometric cross-section of the nanorod, and  $\theta_s$  for the (polar) scattering angle. The power scattered to the far-field, normalized by the incident intensity, namely, the scattering cross-section (SCS), simply reads:

$$\text{SCS}(\omega) = 2\pi \int_{-1}^1 \frac{E_{\theta_s} E_{\theta_s}^*}{|E_0|^2} d(\sin \theta_s) \quad (8)$$

Likewise, the absorption cross-section can be calculated through the expression:

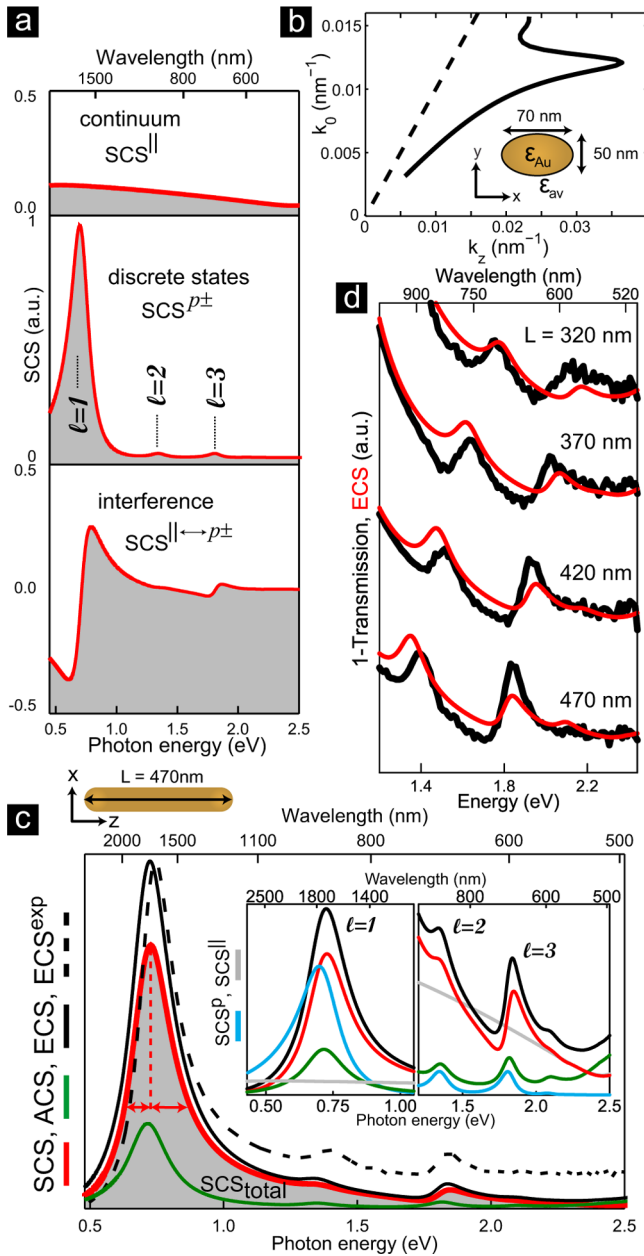


**Figure 4.** 1D line current model. (a) Scattering cross-sections resulting from the nanorod’s forced current ( $SCS^{\parallel}$ ), plasmonic current ( $SCS^{p\pm}$ ), and interference term ( $SCS^{\parallel\leftrightarrow p\pm}$ ). (b) FEM calculated plasmon dispersion of an infinite gold wire with cross-sectional shape as indicated in the inset and used in the model. (c) Comparison between experimental ECS (black dashed line) for  $L = 470$  nm and ACS (green), total SCS (red), and ECS (black full line) computed using the analytical 1D model for a finite gold rod with cross-sectional dimensions as in (b), reflection coefficient  $r = -0.72$ ,  $L = 485$  nm, and  $\theta = 15^\circ$ . Inset: zoom-in on the antenna modes including background  $SCS^{\parallel}$  (gray) and plasmon induced  $SCS^p$  (cyan). (d) 1D model ECS (red lines,  $\theta = 23^\circ$ ) reproducing the experimental ECS (black lines) spectral positions and Lorentzian and Fano line shapes of  $l = 2$  and  $3$  for different rod lengths.

$$\begin{aligned}
 ACS(\omega) &= \text{Re} \int_{V_{\text{rod}}} \frac{\omega \epsilon_r''(\omega) \epsilon_0 n_0 (\mathbf{E}^{(\text{inside})})^* \cdot \mathbf{E}^{(\text{inside})}}{|E_0|^2} dV \\
 &= \frac{S_{\text{rod}}^{xy} \epsilon_r''(\omega)}{k_0 \epsilon_0^2 |\epsilon(\omega)|^2 |E_0|^2} \int_{-L/2}^{L/2} |I(z)|^2 dz \quad (9)
 \end{aligned}$$

where  $\epsilon_r''(\omega)$  is the imaginary part of the relative dielectric function and  $c_0$  the speed of light in vacuum.

Therefore, the plasmon modes and related spectral line shapes originate in this simple antenna model from the current density in eq 2. It follows from the amplitudes of the plasmonic terms  $I_{p\pm}$  that for the particular case where  $r = -1$  plasmonic resonances appear for vanishing  $\sin(k_p(\omega)L) = 0$ :

$$k_p(\omega)L = l\pi, \quad L = l \frac{\lambda_p(\omega)}{2}, \quad l = 1, 2, 3, \dots$$

namely, at nanorod lengths that are multiples of the half-plasmon-wavelength, as expected. In particular, at  $\theta = 0^\circ$ ,  $k_{\parallel} = 0$ , the current density reduces to the simple expression:

$$I(z, \theta = 0^\circ) = I_{\parallel} \left[ 1 - \frac{\cos(k_p(\omega)z)}{\cos(k_p(\omega)L/2)} \right] \quad (10)$$

The latter current yields only odd ( $l = 1, 3, \dots$ ) plasmon resonances at normal incidence with respect to the nanorod axis, even modes being forbidden, as expected from polarization/symmetry arguments and the experimental and simulation results in Figure 2. Recall that odd (even) mode symmetry refers to the charge distribution, manifested as even (odd) current density. It follows from eqs 7 and 8 that the radiation from such odd modes interfere with that of the continuum-like background induced by the illuminating field (first term in the rhs of eq 10), which exhibits the odd symmetry (even current) similar to the odd, lowest-order mode (in turn similar to a half-wavelength antenna pattern). In the case of off-normal incidence, even modes emerge. Nonetheless, such terms exhibit odd current densities proportional to  $\sin(k_p(\omega)z)$  in eq 2, thus leading to vanishing interference with the broad background for near-normal excitation.

The model conveniently allows one to separate the different contributions to the electric far-field (eq 7), and thus to the SCS (eq 8), coming from the various currents flowing in the nanorod. In Figure 4a ( $\theta = 15^\circ$ ), the contributions to the SCS from the forced current  $I_{\parallel}$  (top graph) and the plasmonic currents  $I_{p\pm}$  (middle graph) are plotted. The bottom graph shows the interference term proportional to  $\int (E_{\theta_s} E_{\theta_{s\pm}}^* + E_{\theta_{s\pm}} E_{\theta_s}^*) d(\sin \theta_s)$  which accounts for the interference of the electric far-fields originating from each current. Summing up the background continuum and plasmonic contributions, together with the interference term, one recovers the total SCS, which is plotted in panel c (red line). From the interference term, it is understood that, for the odd modes, at wavelengths shorter than the resonance wavelength, the total SCS increases (constructive interference) while at longer wavelengths the SCS decreases (destructive interference). Note how this decomposition of the nanorod’s scattering components resembles the coupling process illustrated in Figure 1a. The unknown element there was the interference/mixing term represented by the double black arrow.

The total scattering together with eq 9 for the absorption allows a direct comparison of the model predictions for the extinction cross-section (ECS) with the experimental results. In Figure 4c we compare the experimental extinction spectrum of the  $L = 470$  nm rod (black dashed line) with the predictions of the model (black solid line). Also the different contributions to the ECS, namely, the scattering (SCS, red solid line) and the absorption (ACS, green solid line), as obtained from the model, are depicted. Interestingly, the model correctly describes the

fact that for the odd modes the maximum of the ACS is red-shifted with respect to that of the SCS, in agreement with the FEM simulations in Figure 2. The inset shows a zoom-in on modes  $l = 1, 3$  and  $l = 2$  highlighting the, respectively, asymmetry and symmetry and includes the background SCS<sup>ll</sup> (gray line) and plasmonic SCS<sup>p</sup> (cyan line) contributions. All results are normalized to the maximum of the ECS. Figure 4d makes a comparison for the  $l = 2$  and  $l = 3$  resonances between experimental ECS results (black lines) and ECS model predictions (red lines,  $\theta = 23^\circ$ ) for different rod lengths, as in Figure 3. Figure S4 in the Supporting Information shows an extended spectral range including the first-order mode. The spectral positions as well as the Fano and Lorentzian line shapes of the three lowest order antenna modes are very well reproduced. In all line current calculations we have taken a constant reflection coefficient  $r = -0.72$  and an additional length  $L_{\text{add}} = 15$  nm. Both quantities could depend on the wavelength. Equivalently, a complex reflection coefficient could be taken, which is fully justified to be frequency-dependent. This would further improve the agreement. However, such refinements are out of the scope of the present work, and the agreement is already evident by taking only constant values. In the Supporting Information, Figure S5 compares the model predictions with FEM calculations for a silver nanorod indicating the validity of the model for higher-order resonances up to  $l = 6$ .

To summarize, both Fano-type and Lorentzian-type resonant spectral line shapes are experimentally observed in the optical extinction of gold nanorod antennas under near-normal plane wave illumination. Surface plasmon modes of even parity were found to give rise to symmetric Lorentzian line shape, while modes of odd parity present Fano interference with a spectrally broad dipolar background continuum resulting in asymmetric line profiles. The experimental data were verified by finite element simulations. An analytical one-dimensional line current model accurately reproduces the spectral positions and line shapes of the different modes supported by the nanorod antenna and reveals the mechanisms leading to the parity controlled interferences in the scattered light. The occurrence of Fano interference generally affects the in- and out-coupling of light to matter.<sup>48</sup> The presented results therefore have important implications for a wide range of applications using optical nanorod antennas. In V-shaped nanorods, for instance, the Fano interference of the third-order antenna mode gives rise to unidirectional side scattering of a plane wave and unidirectional emission of a quantum emitter.<sup>52</sup> Nanorod heterodimers were recently shown to present plasmon-induced transparency, a phenomenon based on Fano interference, at visible wavelengths.<sup>53</sup> Due to the extreme dispersion and slowing of light, this effect presents great potential for optical information processing and high sensitivity sensing.

## ■ ASSOCIATED CONTENT

### ● Supporting Information

Details about the FEM simulations; effect of a substrate and the angle of incidence on the resonance line shape; FEM simulations including the first-order antenna mode; Figure 4d with extended spectral range including the first order mode; detailed description of the heuristic Fano model fit; 1D line model predictions for higher-order antenna modes. This material is available free of charge via the Internet at <http://pubs.acs.org>.

## ■ AUTHOR INFORMATION

### Corresponding Author

\*E-mail: Niels.Verellen@fys.kuleuven.be.

### Notes

The authors declare no competing financial interest.

## ■ ACKNOWLEDGMENTS

N.V. acknowledges the FWO (Flanders) and D.V. the I.W.T. Flanders for financial support. N.V., D.D., and V.V.M. are supported by the Methusalem funding by the Flemish Government. J.A.S.-G. and R.P.-D. acknowledge the Spanish “Ministerio de Economía y Competitividad”, through the Consolider-Ingenio project EMET (CSD2008-00066) and NANOPLAS+ (FIS2012-31070), and the “Comunidad de Madrid” (grant MICROSERES II P2009/TIC-1476), for financial support. R.P.-D. also acknowledge support from the European Social Fund and CSIC through a JAE-Pre grant. The authors thank Jos Moonens for e-beam assistance, Yannick Sonnefraud and Vincenzo Giannini for their valuable input, and Karen Levrie for graphical support.

## ■ REFERENCES

- (1) Novotny, L.; van Hulst, N. *Nat. Photonics* **2011**, *5*, 83–90.
- (2) Giannini, V.; Fernández-Domínguez, A. I.; Heck, S. C.; Maier, S. A. *Chem. Rev.* **2011**, *111*, 3888–3912.
- (3) Kosako, T.; Kadoya, Y.; Hofmann, H. F. *Nat. Photonics* **2010**, *4*, 312–315.
- (4) Curto, A. G.; Volpe, G.; Taminiau, T. H.; Kreuzer, M. P.; Quidant, R.; van Hulst, N. F. *Science* **2010**, *329*, 930–933.
- (5) Dorfmueller, J.; Dregely, D.; Esslinger, M.; Khunsin, W.; Vogelgesang, R.; Kern, K.; Giessen, H. *Nano Lett.* **2011**, *11*, 2819–2824.
- (6) Dregely, D.; Taubert, R.; Dorfmueller, J.; Vogelgesang, R.; Kern, K.; Giessen, H. *Nat. Commun.* **2011**, *2*, 267.
- (7) Knight, M. W.; Sobhani, H.; Nordlander, P.; Halas, N. J. *Science* **2011**, *332*, 702–704.
- (8) Taminiau, T. H.; Stefani, F. D.; van Hulst, N. F. *Nano Lett.* **2011**, *11*, 1020–1024.
- (9) Curto, A. G.; Taminiau, T. H.; Volpe, G.; Kreuzer, M. P.; Quidant, R.; van Hulst, N. F. *Nat. Commun.* **2013**, *4*, 1750.
- (10) Krenn, J. R.; Schider, G.; Rechberger, W.; Lamprecht, B.; Leitner, A.; Aussenegg, F. R.; Weeber, J. C. *Appl. Phys. Lett.* **2000**, *77*, 3379–3381.
- (11) Schider, G.; Krenn, J. R.; Hohenau, A.; Ditlbacher, H.; Leitner, A.; Aussenegg, F. R.; Schaich, W. L.; Puscasu, I.; Monacelli, B.; Boreman, G. *Phys. Rev. B* **2003**, *68*, 155427.
- (12) Payne, E. K.; Shuford, K. L.; Park, S.; Schatz, G. C.; Mirkin, C. A. *J. Phys. Chem. B* **2006**, *110*, 2150–2154.
- (13) Wei, H.; Reyes-Coronado, A.; Nordlander, P.; Aizpurua, J.; Xu, H. *ACS Nano* **2010**, *4*, 2649–2654.
- (14) Zhang, S.; Chen, L.; Huang, Y.; Xu, H. *Nanoscale* **2013**, *5*, 6985–6991.
- (15) Wang, Y.; Abb, M.; Boden, S. A.; Aizpurua, J.; de Groot, C. H.; Muskens, O. L. *Nano Lett.* **2013**, *13*, 5647–5653.
- (16) Imura, K.; Nagahara, T.; Okamoto, H. *J. Chem. Phys.* **2005**, *122*, 154701.
- (17) Dorfmueller, J.; Vogelgesang, R.; Weitz, T. R.; Rockstuhl, C.; Etrich, C.; Pertsch, T.; Lederer, F.; Kern, K. *Nano Lett.* **2009**, *9*, 2372–2377.
- (18) Schnell, M.; Garcia-Etxarri, A.; Huber, A. J.; Crozier, K.; Aizpurua, J.; Hillenbrand, R. *Nat. Photonics* **2009**, *3*, 287–291.
- (19) Denkova, D.; Verellen, N.; Silhanek, A. V.; Valev, V. K.; Van Dorpe, P.; Moshchalkov, V. V. *ACS Nano* **2013**, *7*, 3168–3176.
- (20) Ghenuche, P.; Cherukulappurath, S.; Taminiau, T. H.; van Hulst, N. F.; Quidant, R. *Phys. Rev. Lett.* **2008**, *101*, 116805.

- (21) Vesseur, E. J. R.; de Waele, R.; Kuttge, M.; Polman, A. *Nano Lett.* **2007**, *7*, 2843–2846.
- (22) Volpe, G.; Noack, M.; Aimovi, S. S.; Reinhardt, C.; Quidant, R. *Nano Lett.* **2012**, *12*, 4864–4868.
- (23) Bosman, M.; Keast, V. J.; Watanabe, M.; Maarroof, A. I.; Cortie, M. B. *Nanotechnology* **2007**, *18*, 165505.
- (24) Barnard, E. S.; Pala, R. A.; Brongersma, M. L. *Nat. Nanotechnol.* **2011**, *6*, 588–593.
- (25) Novotny, L. *Phys. Rev. Lett.* **2007**, *98*, 266802.
- (26) Khlebtsov, B. N.; Khlebtsov, N. G. *J. Phys. Chem. C* **2007**, *111*, 11516–11527.
- (27) Bryant, G. W.; Garcia de Abajo, F. J.; Aizpurua, J. *Nano Lett.* **2008**, *8*, 631–636.
- (28) Reed, J. M.; Wang, H.; Hu, W.; Zou, S. *Opt. Lett.* **2011**, *36*, 4386–4388.
- (29) López-Tejiera, F.; Paniagua-Domínguez, R.; Rodríguez-Oliveros, R.; Sánchez-Gil, J. A. *New J. Phys.* **2012**, *14*, 023035.
- (30) López-Tejiera, F.; Paniagua-Domínguez, R.; Sánchez-Gil, J. A. *ACS Nano* **2012**, *6*, 8989–8996.
- (31) Zia, R.; Brongersma, M. L. *Nat. Nanotechnol.* **2007**, *2*, 426–429.
- (32) Luk'yanchuk, B.; Zheludev, N. I.; Maier, S. A.; Halas, N. J.; Nordlander, P.; Giessen, H.; Chong, C. T. *Nat. Mater.* **2010**, *9*, 707–715.
- (33) Giannini, V.; Francescato, Y.; Amrania, H.; Phillips, C. C.; Maier, S. A. *Nano Lett.* **2011**, *11*, 2835–2840.
- (34) Fan, J. A.; Wu, C.; Bao, K.; Bao, J.; Bardhan, R.; Halas, N. J.; Manoharan, V. N.; Peter, N.; Shvets, G.; Capasso, F. *Science* **2010**, *328*, 1135–1138.
- (35) Zhang, S.; Genov, D. A.; Wang, Y.; Liu, M.; Zhang, X. *Phys. Rev. Lett.* **2008**, *101*, 047401.
- (36) Verellen, N.; Sonnefraud, Y.; Sobhani, H.; Hao, F.; Moshchalkov, V. V.; Van Dorpe, P.; Nordlander, P.; Maier, S. A. *Nano Lett.* **2009**, *9*, 1663–1667.
- (37) Hao, F.; Sonnefraud, Y.; Van Dorpe, P.; Maier, S. A.; Halas, N. J.; Nordlander, P. *Nano Lett.* **2008**, *8*, 3983–3988.
- (38) Sonnefraud, Y.; Verellen, N.; Sobhani, H.; Vandenbosch, G. A. E.; Moshchalkov, V. V.; Van Dorpe, P.; Nordlander, P.; Maier, S. A. *ACS Nano* **2010**, *4*, 1664–1670.
- (39) Verellen, N.; Van Dorpe, P.; Huang, C.; Lodewijks, K.; Vandenbosch, G. A. E.; Lagae, L.; Moshchalkov, V. V. *Nano Lett.* **2011**, *11*, 391–397.
- (40) Verellen, N.; Van Dorpe, P.; Vercruyssen, D.; Vandenbosch, G. A. E.; Moshchalkov, V. V. *Opt. Express* **2011**, *19*, 11034–11051.
- (41) Poddubny, A. N.; Rybin, M. V.; Limonov, M. F.; Kivshar, Y. S. *Nat. Commun.* **2012**, *3*, 914.
- (42) Zhang, S.; Bao, K.; Halas, N. J.; Xu, H.; Nordlander, P. *Nano Lett.* **2011**, *11*, 1657–1663.
- (43) Chen, H.; Shao, L.; Ming, T.; Woo, K. C.; Man, Y. C.; Wang, J.; Lin, H.-Q. *ACS Nano* **2011**, *5*, 6754–6763.
- (44) Hopkins, B.; Poddubny, A. N.; Miroshnichenko, A. E.; Kivshar, Y. S. *Phys. Rev. A* **2013**, *88*, 053819.
- (45) Papisimakis, N.; Zheludev, N. I. *Opt. Photonics News* **2009**, *20*, 22–27.
- (46) Douillard, L.; Charra, F.; Korczak, Z.; Bachelot, R.; Kostcheev, S.; Lerondel, G.; Adam, P.-M.; Royer, P. *Nano Lett.* **2008**, *8*, 935–940.
- (47) Dorfmueller, J.; Vogelgesang, R.; Khunsin, W.; Rockstuhl, C.; Etrich, C.; Kern, K. *Nano Lett.* **2010**, *10*, 3596–3603.
- (48) Miroshnichenko, A. E.; Flach, S.; Kivshar, Y. S. *Rev. Mod. Phys.* **2010**, *82*, 2257–2298.
- (49) Johnson, P. B.; Christy, R. W. *Phys. Rev. B* **1972**, *6*, 4370.
- (50) Avrutsky, I.; Gibson, R.; Sears, J.; Khitrova, G.; Gibbs, H. M.; Hendrickson, J. *Phys. Rev. B* **2013**, *87*, 125118.
- (51) Gallinet, B.; Martin, O. J. F. *Phys. Rev. B* **2011**, *83*, 235427.
- (52) Vercruyssen, D.; Sonnefraud, Y.; Verellen, N.; Fuchs, F. B.; Di Martino, G.; Lagae, L.; Moshchalkov, V. V.; Maier, S. A.; Van Dorpe, P. *Nano Lett.* **2013**, *13*, 3843–3849.
- (53) Biswas, S.; Duan, J.; Nepal, D.; Park, K.; Pachter, R.; Vaia, R. A. *Nano Lett.* **2013**, *13*, 6287–6291.